Qian et al. *Microsystems & Nanoengineering* (2026)12:352
https://doi.org/10.1038/s41378-026-01474-z

Microsystems & Nanoengineering
www.nature.com/micronano

ARTICLE Open Access

Focusing and weighing microanalytes in liquid enabled by higher-order piezoelectric resonant membranes

Jingui Qian[1,2], Wenqi Fan[1], Sheng Tang[1], Cheng Guo[1], Xiangyang Wang[3], Mengyu Huang[1], Guoqiang Wu[3]✉ and Joshua E.-Y. Lee[4,5]✉

Abstract

Micro-electromechanical-system (MEMS) resonators have been recognized as powerful tools for precision mass detection. However, achieving both flexible on-chip capture of microanalytes and high-sensitivity liquid-phase sensing remains a technical challenge. We present a fully anchored multi-modal piezoelectric resonant membrane (PRM) that utilizes self-excited bulk acoustic waves to rapidly enrich sparsely dispersed microparticles within milliliter droplets and precisely locate them at the region of highest vibrational amplitude — the most sensitive area for resonance detection. The design of higher-order resonance modes preserves acoustofluidic enrichment performance while enabling reconfigurable particle distribution patterns through modulation of the acoustic field distribution. Experimental results demonstrate that the resonant frequency shift induced by the same mass load increases with the mode order, indicating that the sensing sensitivity is proportional to the resonance order. We systematically characterized the acoustofluidic parameters and electrical measurement performance of transverse modes from (0, 0) to (4, 0). This work shows that extending the integrated actuation-and-sense approach to consider multiple modes of resonances presents a toolbox for designing such miniaturized platforms to address nanogram-level mass analysis in liquid phase.

Introduction

High-sensitivity and high-precision detection of microanalytes in liquid-phase environments holds significant value in critical fields such as biomedical diagnosis, pharmaceutical quality control, environmental monitoring[1], and food safety assessment. In the pharmaceutical industry, for example, liquid-phase microanalysis enables the quantitative characterization of active ingredients, microanalyte detection of impurities, and real-time quality control during production. This technology provides essential support for drug research and development, as well as large-scale manufacturing processes. Micro/nano electromechanical (M/NEM) resonators, which serve as core sensor devices in this field, have become a research focus due to their high-precision processing capabilities, potential for large-scale production, and ultra-high sensitivity[2]. These resonators detect analytes by measuring shifts in resonant frequency caused by mass loading. Their mass resolution can reach the attogram (ag) level[3,4] or even lower, significantly surpassing that of traditional detection techniques, thus enabling the analysis of microanalyte targets, such as single molecules and individual cells.

Despite their promising potential, the practical implementation of M/NEMS resonators in liquid-phase environments faces two primary challenges[5]. The first challenge lies in effectively concentrating microanalytes onto the resonator surface. Given that sample droplets (typically 2–3 mm diameter) often exceed the resonator

Correspondence: Guoqiang Wu (wuguoqiang@whu.edu.cn) or Joshua E.-Y. Lee (joshua.lee@uts.edu.au)
[1]Anhui Province Key Laboratory of Measuring Theory and Precision Instrument, School of Instrument Science and Opto-Electronics Engineering, Hefei University of Technology, Hefei, China
[2]State Key Laboratory of Millimeter Waves, Southeast University, Nanjing, China
Full list of author information is available at the end of the article

© The Author(s) 2026
Open Access This article is licensed under a Creative Commons Attribution-NonCommercial-NoDerivatives 4.0 International License, which permits any non-commercial use, sharing, distribution and reproduction in any medium or format, as long as you give appropriate credit to the original author(s) and the source, provide a link to the Creative Commons licence, and indicate if you modified the licensed material. You do not have permission under this licence to share adapted material derived from this article or parts of it. The images or other third party material in this article are included in the article's Creative Commons licence, unless indicated otherwise in a credit line to the material. If material is not included in the article's Creative Commons licence and your intended use is not permitted by statutory regulation or exceeds the permitted use, you will need to obtain permission directly from the copyright holder. To view a copy of this licence, visit http://creativecommons.org/licenses/by-nc-nd/4.0/.

dimensions by orders of magnitude, developing active mechanisms to capture and enrich analytes in fluid media would significantly enhance detection sensitivity. Previously, we proposed a dual-chip integration strategy combining lithium niobate-based surface acoustic wave (SAW) devices with piezoelectric MEM resonators, offering an innovative solution that integrates acoustic manipulation and in-situ liquid-phase mass sensing in droplets on a single platform[6]. Recently, we demonstrated a piezoelectric micro-mechanical diaphragm resonator that successfully integrated these functions through the inverse and direct piezoelectric effects of aluminum nitride (AlN)[7]. The device employed a fully anchored, sealed diaphragm structure operating in a transverse vibration mode, generating localized acoustic radiation forces under high-voltage excitation. These forces concentrate microanalytes at vibration antinodes where acoustic trapping occurs. Liquid-phase sensing was then performed by reducing the excitation voltage, maintaining the same vibration mode to measure mass-loading effects. This "control-and-sense" design ensures analyte trapping and sensing occur at the device's most sensitive regions, effectively addressing the issues of uneven analyte distribution and low capture efficiency in conventional devices. The fully differential configuration further suppresses parasitic feedthrough, enhancing signal integrity that is compromised especially when measuring in a liquid[8–12].

The second major challenge involves reducing the insertion loss of the measured electromechanical resonance (e.g., transmission curves) especially when measuring in the liquid phase. First, fluidic viscous damping significantly reduces the device quality factor (Q), increasing energy dissipation and directly limiting mass resolution and signal-to-noise ratio[13–16]. Second, the high dielectric properties of liquid media induce substantial parasitic feedthrough effects that obscure characteristic electrical signals[17,18]. While strategies such as piezoelectric transducer optimization and vibration mode engineering[19–24] have partially mitigated these issues, most of the research has focused purely on the resonator characteristics with no due consideration of compatibility for acoustic actuation. Notably, not all MEM resonant structures can effectively generate acoustofluidic forces on the device surface. Low-frequency/order diaphragm resonators, though capable of liquid-phase analyte enrichment, exhibit limited sensitivity due to small frequency shifts. The theoretical approach of reducing resonator cavity dimensions to increase resonance frequency in gas-phase applications is inapplicable to liquid-phase sensing, as key performance parameters like Q and motional resistance are adversely affected by dimensional scaling. Therefore, introducing diverse vibration modes (e.g., higher-order diaphragm resonances) represents the next step in the effort to enhance microanalyte detection sensitivity in liquid environments, while simultaneously enabling differentiated acoustic streaming manipulation effects for precise capture of analytes.

In this work, we propose a fully anchored multi-modal PRM and extensively evaluate its acoustic enrichment capabilities and liquid-phase sensing performance across multiple resonant modes. Through systematic analysis of acoustic enrichment efficiency and single-cycle duration under varying operational parameters, we establish quantitative relationships between these performance metrics and critical factors, including resonant mode, particle size, analyte concentration, and input voltage. Given the statistically significant difference in resonance frequency offset between sparsely distributed particles and acoustically enriched particles, demonstrating that acoustic localization is essential for enhancing detection sensitivity[25]. Our experiment's findings reveal a fundamental trade-off between different vibration modes in liquid-phase sensing. While the highest-order transverse (4, 0) mode demonstrates exceptional energy efficiency with high Q and low motional resistance, the lower-order transverse (3, 0) mode excels in signal fidelity through superior parasitic feedthrough suppression. This discovery highlights the critical design consideration for mode selection: high-sensitivity applications may prioritize the (4, 0) mode's energy efficiency, whereas systems requiring robust signal discrimination would benefit from the (3, 0) mode's enhanced noise suppression capabilities. The high-order mode PRM, through the integration of acoustic enrichment and mass sensing functions[26,27], overcomes the performance limitations of traditional M/NEM resonators in liquid-phase environments. Its outstanding detection sensitivity, signal stability, and ease of operation offer novel technical solutions for mass sensing in liquid phase, which demonstrate significant potential for both practical applications and industrialization[28–34].

Materials and methods

Conceptualization of the PRM

A multi-modal PRM was designed with a fully anchored TPoS (thin-piezoelectric-film-on-silicon) structure, which has a high degree of stability and protects the leakage of liquid from top to bottom. Figure 1a illustrates the deformation of the membrane and the resulting particle enrichment under the transverse (4, 0) resonance mode (as the chosen example for reference), contrasted against the initial state of randomly dispersed particles within the micro-droplets depicted in Fig. 1b. As illustrated, the (4, 0) mode PRM features eight 45° sector electrodes to preferentially excite the (4, 0) transverse resonance mode[8]. To execute acoustofluidic particle manipulation, the piezoelectric transducer converts the input RF signal into output acoustic waves, driving the

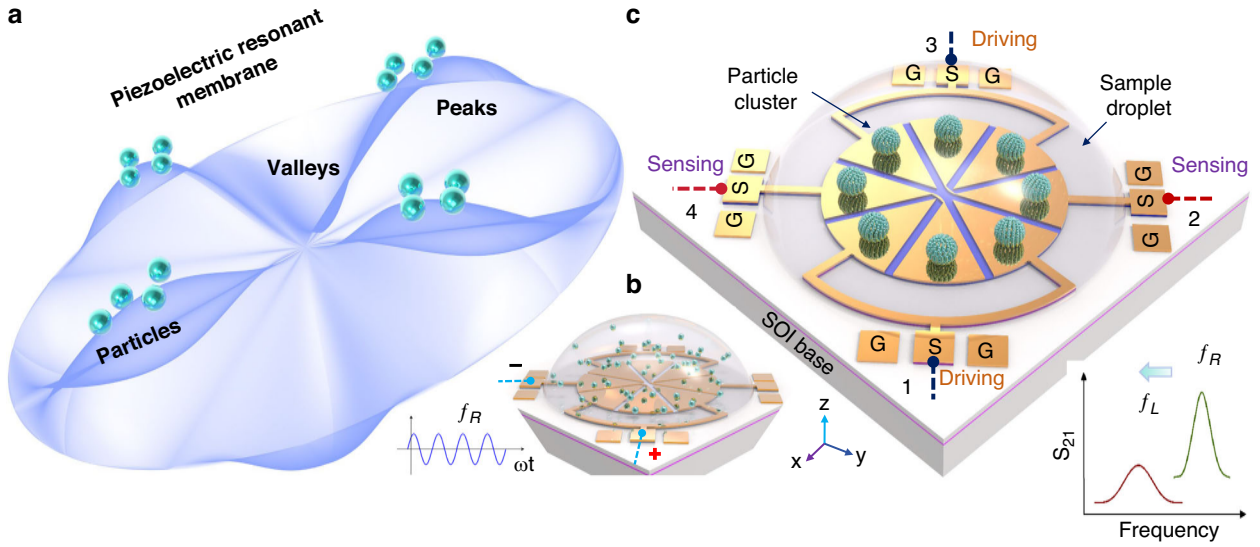

Fig. 1 Conceptualization of the PRM for manipulating and sensing the microanalytes in liquid phase. a Schematic diagram of the PRM diaphragm deformation, illustrating the particle enrichment under the transverse (4, 0) mode. **b** Perspective view of the PRM after the addition of a micro-droplet containing sparse particles. **c** Perspective view of the PRM after loading acoustic-focused particle cluster in micro-droplet, accompanied by a schematic diagram showing the resulted frequency shift before and after particle aggregation, as well as the schematic of the electrical connection for fully differential configuration

diaphragm to resonate mostly strongly in the (4, 0) transverse mode. To actuate the (4, 0) mode, a pair of adjacent sector electrodes was driven by a single-ended signal (i.e., one electrode connected to ground), producing highly localized acoustic waves that interact directly with the micro-droplets on the PRM. This direct and proximal interaction between the waves and droplets minimizes propagation loss in contrast to typical SAW acoustic tweezers characterized by long-distance propagation of acoustic waves through the liquid medium. When the particles have been sorted into place, the RF signal is switched off to conclude the actuation phase. Next, in the sensing phase, to characterize the perturbed resonant frequency of the PRM (due to particle loading), we excited a pair of adjacent sector electrodes using a balanced pair of differential voltages, sweeping the frequency within the span of the resonance frequency. The resonance is sensed through another pair of adjacent electrodes based on the direct piezoelectric effect, whereby the two adjacent sector electrodes create opposing field polarities in response to the mechanical strain field associated with the (4, 0). The pair of opposing polarities was detected as differential currents. In short, the actuation phase clusters the initially dispersed particles in the regions of highest transverse displacement amplitude, while the sensing phase calibrates the effect of the associated mass loading by comparing against the resonance frequency measured for a liquid with no particles.

Simulation and design of the PRMs

Finite element (FE) simulations were performed using commercial COMSOL 6.0 software, with a film radius of 280 μm, and accounting for 30 μm cavities created by etching during the manufacturing process. Figure 2a illustrates the relative deformation profiles of a vibrating circular membrane exhibiting transverse (n, 0) modes with $n = 0$ to 4. The (0, 0) mode represents fundamental vibration characterized by maximal amplitude at the membrane's center, with a simulated air-coupled resonant frequency of 0.55 MHz. The (1, 0) mode divides the membrane into two semi-circular vibration regions (π-phase opposition), each achieving peak amplitude at its respective center and displaying a simulated resonant frequency of 1.14 MHz. This pattern continues with increasing nodal complexity: the (2, 0) mode forms four 90° quadrants (1.82 MHz), the (3, 0) mode creates six 60° sectors (2.71 MHz), and the (4, 0) mode produces eight 45° segments (3.69 MHz). Each subsequent mode maintains the principle of maximal amplitude at sector centers while maintaining π-phase differences between adjacent vibration regions, demonstrating a systematic progression in both spatial division and resonant frequency with increasing mode order.

Fabrication of the PRMs

Figure 2b illustrates the micro-fabrication process of the PRMs, while also providing a cross-sectional view of the multilayer structure of a PRM with a diameter of

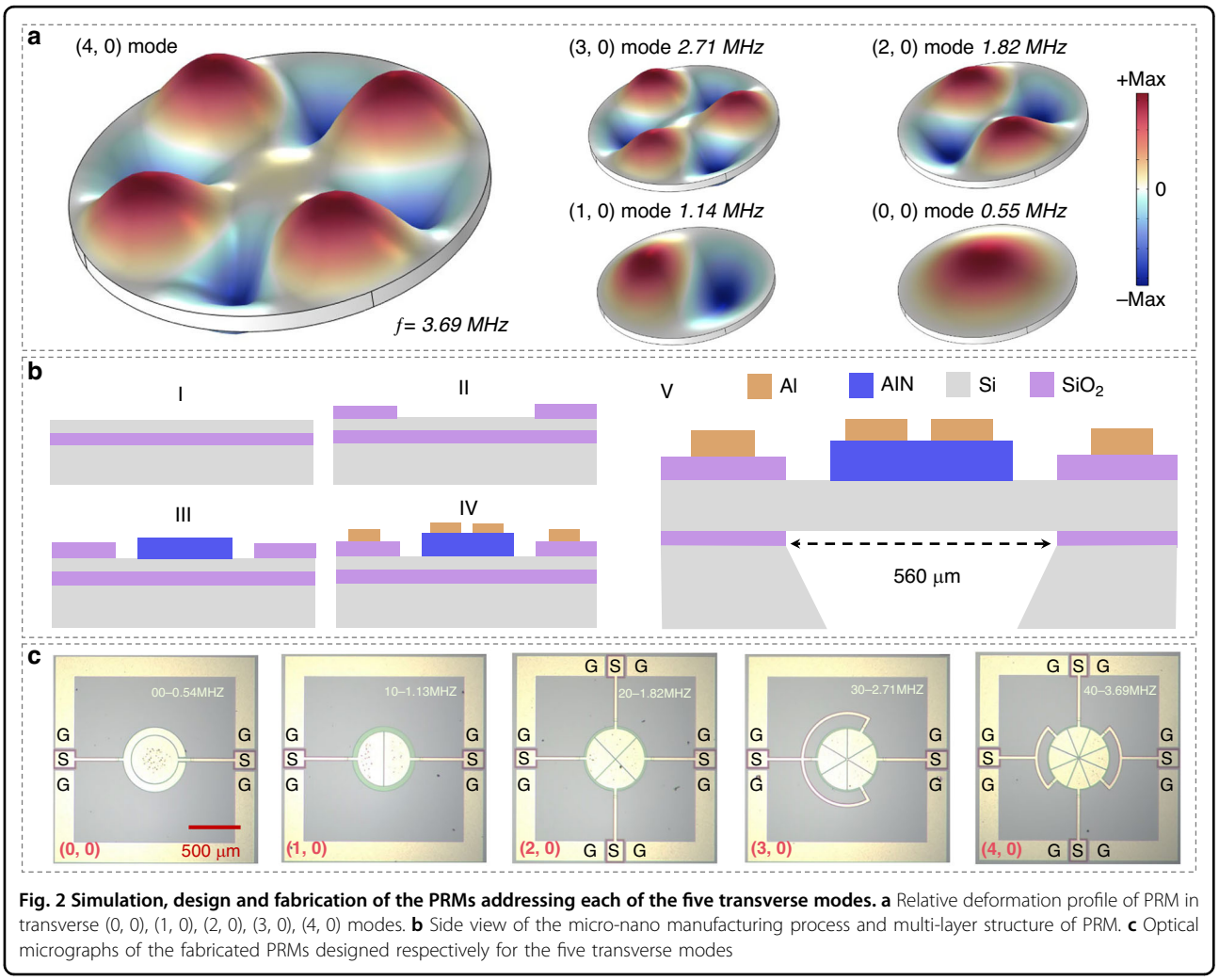

Fig. 2 Simulation, design and fabrication of the PRMs addressing each of the five transverse modes. a Relative deformation profile of PRM in transverse (0, 0), (1, 0), (2, 0), (3, 0), (4, 0) modes. **b** Side view of the micro-nano manufacturing process and multi-layer structure of PRM. **c** Optical micrographs of the fabricated PRMs designed respectively for the five transverse modes

560 μm. Additionally, Fig. 2c provides a top view physical photo of the fabricated PRM in the transverse (n, 0) modes with $n = 0$ to 4 as observed under an optical microscope. The PRM is fabricated using a standard PiezoMUMPs process based on a silicon-on-insulator (SOI) wafer that contains a 400 μm thick silicon substrate, a 1 μm thick buried oxygen layer, and a 10 μm thick silicon device layer. First, a 0.2 μm thick silica layer is thermally grown on the SOI wafer, and then the design pattern is etched by a reactive ion etching process. A 0.5 μm thick AlN layer was deposited by magnetron sputtering and patterned by wet etching. Then a chromium/aluminum (Cr/Al) metal layer (thickness of 20 nm/1000 nm respectively) is deposited, and the contact pad and electrode are formed after graphic processing. Finally, the hydrofluoric acid-based etching process is used to etch the buried oxygen layer, and then the cavity preparation of the back side of the wafer is carried out by the deep reactive ion etching process, and finally, the thin film structure defined by the silicon device layer is released. Three PRM chip dies verify repeatability in electrical, acoustofluidic and mass sensing measurements. Minor batch-to-batch resonant frequency differences arise from backside cavity fabrication variations.

Theoretical analysis of the PRM

Figure 3a presents a typical equivalent circuit diagram to characterize the electrical characteristics of a resonator. Resonant elements (R_m, C_m, L_m) model and capture the electromechanical "motional" characteristics of the resonator (See S1). In general, a resonator can be modeled as a mass-damper-spring mechanical resonance system. The resonant frequency of the PRM is given by the following formula:

$$f_0 = \frac{1}{2\pi}\sqrt{\frac{k}{m}} \tag{1}$$

where the m represents the dynamic mass and k represents the spring constant[35]. In this scenario, the

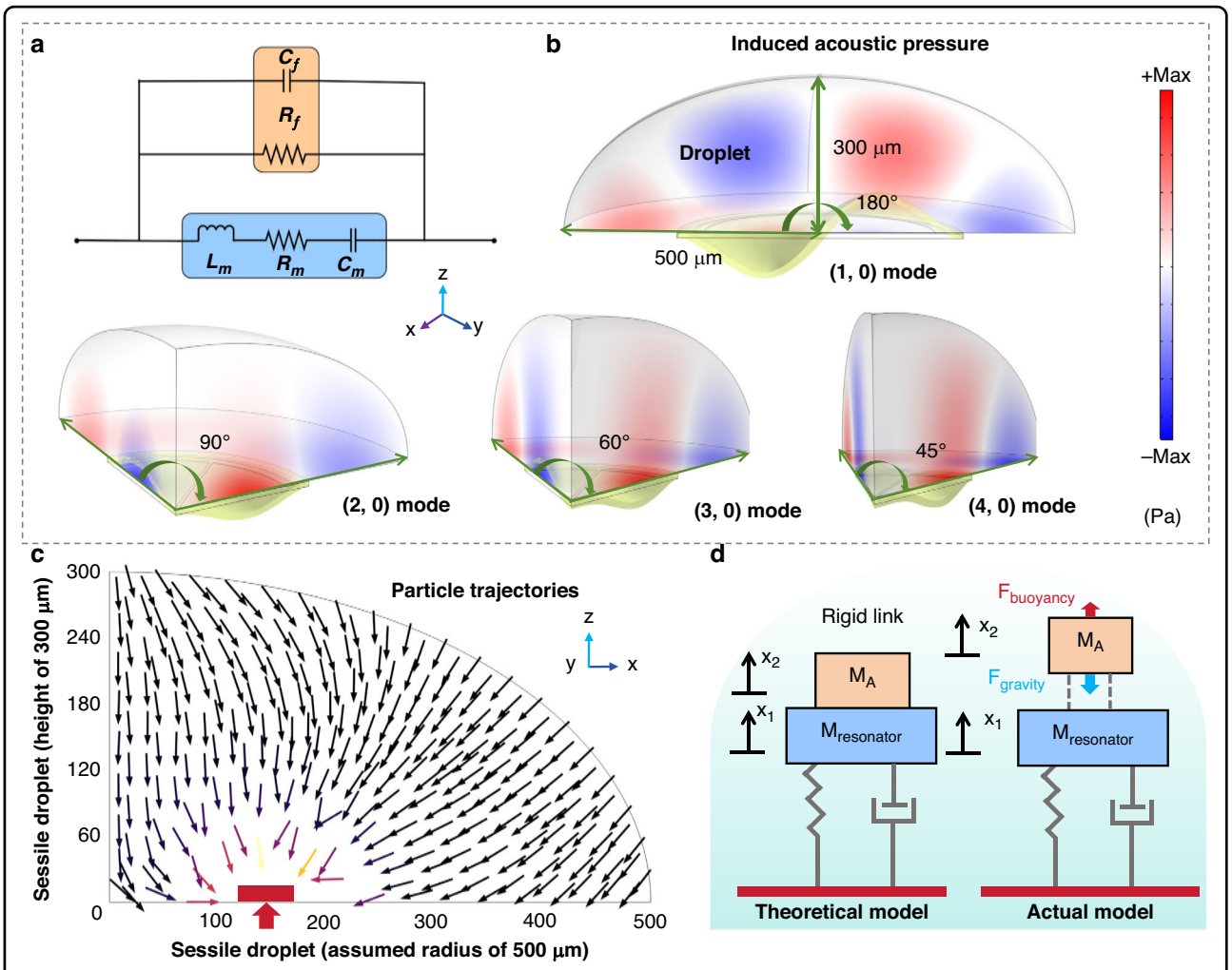

Fig. 3 Theoretical analysis of the PRM for manipulation and sensing of microanalytes. a Electrical equivalent circuit model of a resonator. **b** Acoustic pressure profiles induced by resonance in droplets under PRM transverse modes (1, 0), (2, 0), (3, 0) and (4, 0). **c** Simulation model of particle trajectories in droplets under acoustic radiation force (applied along the thick red line), showing the motion direction and velocity of particles. **d** Two force analysis models of microanalytes loaded on the PRM that characterized as a mass-damper-spring system

transverse bending mode is excited by the input RF signal, generating an acoustic pressure field on the film that induces gradient forces within the droplet, causing particle movement. The acoustic radiation force drives the particles toward the central region of each sector electrode, pulling them down to the resonator surface. This behavior is characteristic of acoustofluidic enrichment and is commonly utilized in various acoustic tweezer devices. We selected particle materials with a density greater than that of water (i.e., media containing denser particles), ensuring their inertia exceeds the buoyancy force of the water. The attractive forces between the particles further facilitate the adhesion of additional particles to the resonator surface, ensuring that particle aggregates remain attached to the PRM electrodes even after the acoustic wave is turned off[36,37]. Consequently, the load induced on the PRM results in a resonant frequency shift, leading to a frequency decrease compared to the condition of pure deionized water.

The core mechanism of PRM-enabled acoustic enrichment was further elaborated based on the aforementioned resonance principle. A gradient radiation force generated from the cyclical fluctuation of acoustic pressure fields will drive the microanalytes to migrate toward the locally minimum acoustic potential wells. When the PRM diaphragm operates in the transverse mode, the regions of largest deflection and pressure coincide at the central position of each electrode. Conversely, the regions of minimal deflection and pressure correspond synchronously at the clamped boundaries of the diaphragm and along the lines of inflexion within the diaphragm. This spatial distribution characteristic of the pressure field

enables a maximum acoustic potential gradient to be established between the regions of maximum and minimum pressure. The gradient radiation force F_r is a negative gradient of the time averaged acoustic potential U, which can be described as following,

$$F_r = -\nabla U \tag{2}$$

$$\mathrm{U} = -\left(\frac{4\pi r^3}{3}\right)\left(\frac{f_1}{2}k_m < p_n^2 > -\frac{3f_2}{4}\rho_m < v_n^2 >\right) \tag{3}$$

where r is the particle radius, p_n is the pressure amplitude, v_n is the acoustic velocity, the monopole term f_1, and the dipole term f_2, which are given by:

$$f_1 = 1 - \frac{k_p}{k_m} \tag{4}$$

$$f_2 = \frac{2(\rho_p - \rho_m)}{2\rho_p + \rho_m} \tag{5}$$

where k_p and ρ_p denote the compressibility and density of the microanalytes, respectively, while k_m and ρ_m correspond to the compressibility (Pa^{-1})and density (gcm^{-3})of the fluid medium. Combining Eqs. (3) to (5), it can be deduced that when the density of the microanalytes is higher than or at least equal to that of the fluid medium, the particles will be trapped in the regions of maximum pressure (i.e., the positions of locally minimum acoustic potentials). The polystyrene (PS) $\rho = 1.05$ (gcm^{-3}),and SiO_2 $\rho = 2$ (gcm^{-3}) particles (purchased from Zhichuan Technology, Jiangsu, China) adopted in this work satisfy this condition; therefore, the central region of each electrode can serve as a stable particle trapping site. Hence, by exciting the PRM to operate in the transverse mode, the microanalytes would be precisely driven to the central region of each sector electrode under the synergistic effect of gradient radiation force and viscous drag force, eventually establishing stable contact with the surface of each electrode. It is important to note that while particle migration is predominantly attributed to acoustic radiation force and pressure maxima, additional factors may also play a role in sessile droplet systems. These include acoustic streaming, capillary effects, evaporation-induced convective flows, particle-particle interactions, adhesion forces, thermal gradients, and electrostatic effects[38]. The quantitative interplay of these mechanisms remains to be systematically characterized in future studies.

To simulate the acoustic field distribution generated by transverse modes resonant deformation of the bottom PRM, we established a geometric model of the droplet with a height of 300 μm and a radius of 500 μm. Figures 3b and S2 show the tangential acoustic pressure profiles within respective droplets centered on two adjacent fan-shaped electrodes enabled by transverse resonance modes from (1, 0) to (4, 0). Referring to the acoustic pressure profiles, we infer that particles aggregate at the peaks and troughs of resonant waves. We construct a simple axisymmetric model that describes acoustic-driven particle enrichment trajectories from the cross-section of the droplet resting on the center of the fan-shaped electrode, as displayed in Fig. 3c. To simulate the acoustic radiation force arising from deformation of the underlying vibrating diaphragm, Z-direction wave excitation is imposed on the bottom boundary of the water droplet over the range of 127 μm to 177 μm. The orientation of each arrow indicates the direction of particle movement, arrow color corresponds to velocity magnitude, and arrow patterns verify that particles aggregate and localize at locations with maximum acoustic pressure.

As illustrated in Fig. 3d, the physical interface between loaded microanalytes and the resonator surface exhibits two distinct coupling modes: rigid and buoyant connections. In rigid coupling, the load material solely increases the resonator's mass, lowering the resonance frequency without altering stiffness or damping (i.e., no relative displacement between particles and resonator). Conversely, buoyant coupling occurs when acoustic loads in sessile droplets experience both buoyancy and gravity, deviating from rigid-link assumptions. Here, the effective mass is governed by buoyant weight rather than the dry inertial mass of analytes. This distinction can be quantified through resonant frequency shifts during acoustic focusing, as frequency changes correlate with buoyant mass loading. This work employs the buoyant model since no rigid connection exists between loaded materials and the PRM electrode surface.

Results and discussion

Electrical measurement of the PRMs

Due to the excessively low resonant frequency of the transverse (0, 0) mode, we were unable to measure its resonant frequency in water, thus preventing a direct comparison. Therefore, we only conducted electrical characterization of the PRM frequency responses in the transverse modes from (1, 0) to (4, 0) using a network analyzer (T5260C-265, Transcom Instruments, China) after the whole MEMS chip was mounted on a probe station (YB600-A, Yingbo, China). Figure 4a, c presents Laser Doppler vibrometer (LDV, UHF-120, Polytec, Germany) mode measurements of these piezoelectric films in air and liquid phase, revealing consistent mode shapes under both environments. It can be observed that for the transverse (1, 0) and (3, 0) modes, connection to the device required two ground-signal-ground (GSG) probes, while for the transverse (2, 0) and (4, 0) modes,

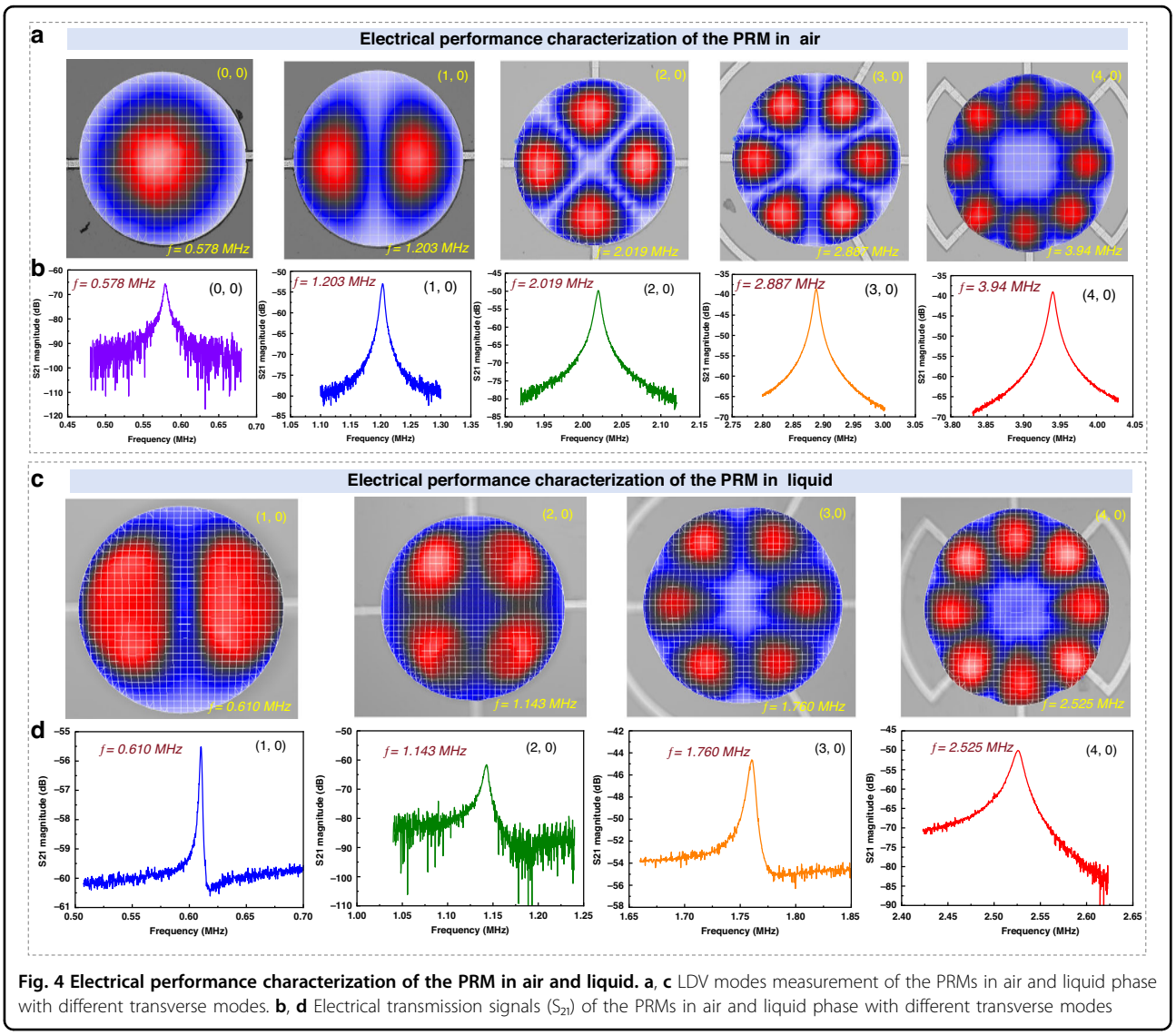

Fig. 4 Electrical performance characterization of the PRM in air and liquid. a, **c** LDV modes measurement of the PRMs in air and liquid phase with different transverse modes. **b**, **d** Electrical transmission signals (S_{21}) of the PRMs in air and liquid phase with different transverse modes

connection necessitated four GSG probes and two power splitters (ZFSCJ-2-2-S, Mini-circuits, USA). Initially, the frequency response of the PRM was measured in air for each transverse mode, and subsequently, the frequency response in water was measured after applying a 0.4 μL droplet of deionized water (e.g., manual pipetting volume errors < ±10%) onto the chip. Notably, as demonstrated in S3, the droplet size does not influence S_{21} measurements provided that the device is fully covered in liquid. The results, as shown in Fig. 4b, d, reveal that the resonant frequency of the PRM in water is significantly lower than that in air, with a reduction of approximately 36–50% in water. This is because when the resonator is immersed in liquid, fluid–structure interaction occurs between the elastic microstructure and the surrounding fluid[39]. The inertia of the surrounding fluid generates added mass, which markedly reduces the resonant frequency of the device and acts as the dominant factor for frequency shift. Viscous damping originating from fluid viscosity dissipates the vibrational energy of the resonator, and their combined effect leads to the evident resonant frequency reduction observed in water.

The lumped parameters for each device under test were extracted by curve fitting the measurement data to the equivalent circuit model. These parameters (e.g., including power consumption) and calculation methods are summarized in S1. We found that the PRM with a diameter of 560 μm demonstrates exceptional liquid-phase electromechanical performance across the transverse (2, 0), (3, 0), and (4, 0) modes. Specifically, it exhibits a high Q and low R_m, both of which are key performance indicators for liquid-phase high-sensitivity mass sensing. Among these modes, the transverse (4, 0) mode shows the best overall performance, with a liquid-phase Q of 247,

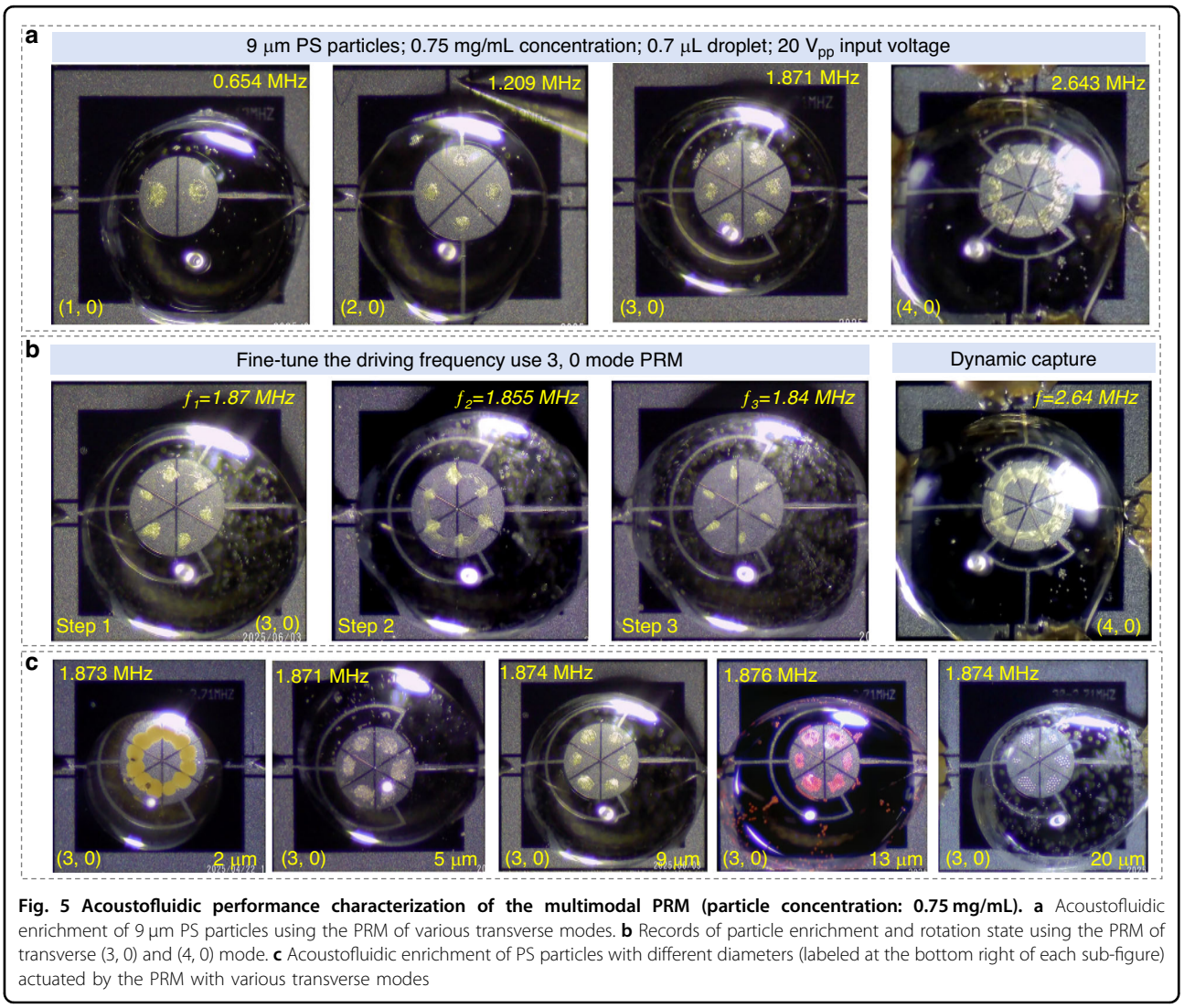

Fig. 5 Acoustofluidic performance characterization of the multimodal PRM (particle concentration: 0.75 mg/mL). a Acoustofluidic enrichment of 9 μm PS particles using the PRM of various transverse modes. **b** Records of particle enrichment and rotation state using the PRM of transverse (3, 0) and (4, 0) mode. **c** Acoustofluidic enrichment of PS particles with different diameters (labeled at the bottom right of each sub-figure) actuated by the PRM with various transverse modes

indicating minimal energy dissipation in viscous liquid environments. Additionally, its dynamic resistance is as low as 31.69 kΩ, facilitating efficient signal transmission and minimizing transmission losses. These data provide critical criteria for modal selection design. The (0, 0) mode fails to detect signals in liquid phases. The (1, 0) and (2, 0) modes suffer from significant performance limitations, with signal quality severely degraded by interference. In contrast, the (3, 0) mode exhibits superior noise suppression capabilities and delivers the optimal signal quality. The (4, 0) mode, meanwhile, demonstrates a high Q and enhanced sensitivity. Accordingly, the (3, 0) mode is recommended for stable signal measurements, while the (4, 0) mode is preferred for high-sensitivity detection tasks. These insights establish a foundational framework for mode engineering in liquid-phase resonant sensing, warranting further systematic investigation into performance optimization strategies.

Reconfigurable acoustofluidic enrichment

To prepare the particle sample, we used a pipette (JOAN LAB, 10 μL, China) to add 1 mL of deionized water to a test tube, followed by the addition of 30 μL of PS particles at a concentration of 25 mg/mL. After shaking thoroughly, a PS solution with a concentration of 0.75 mg/mL was obtained. The transverse (1, 0) and (3, 0) modes can be directly driven by inputting RF signals from a signal generator, whereas the transverse (2, 0) and (4, 0) modes are driven by a differential input RF signal from the signal generator to a pair and two pairs of adjacent sector electrodes. A 0.7 μL droplet of diluted PS solution was applied to the chip, and the frequency of the input signal was adjusted to slightly below the resonant frequency in pure water, since the slight deviations caused by the potential presence of scarce particle loads. The results of microparticle enrichment induced by the self-excited Lamb waves generated by the PRM are depicted in Fig. 5a. It is

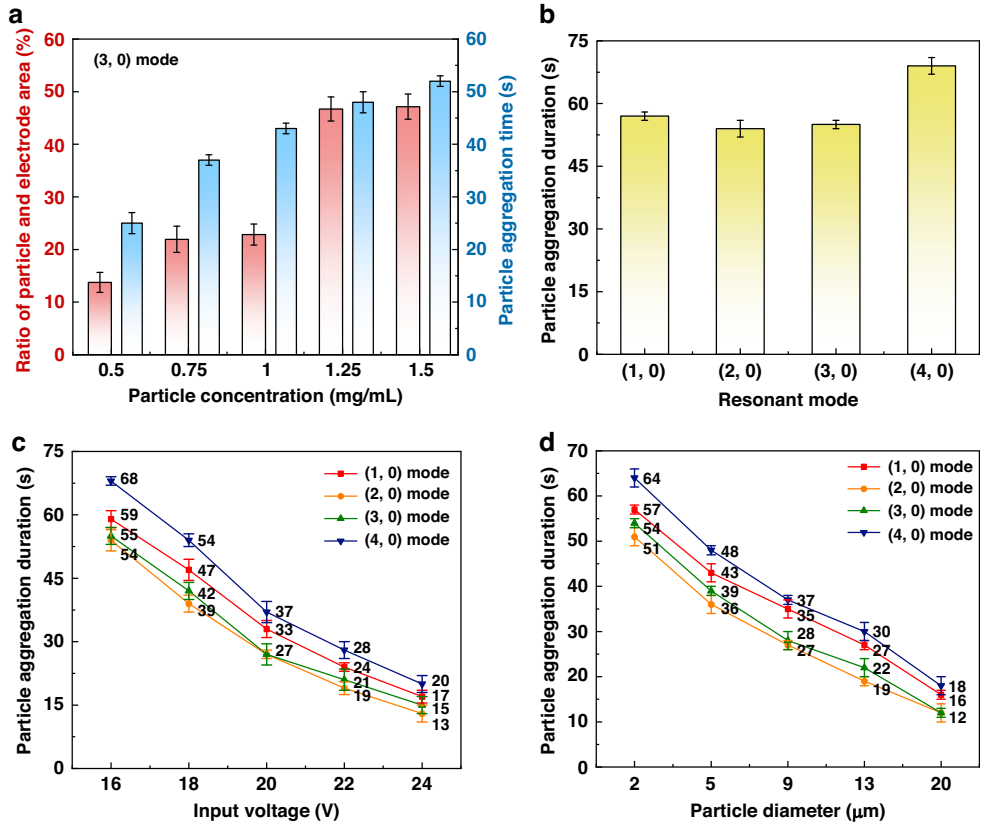

Fig. 6 Acoustofluidic performance characterization implemented by PRM using same samples and driving conditions (e.g., 9 μm diameter PS particle with 0.75 mg/mL concentration under an input voltage of 20 V_{pp}). a The duration of acoustic enrichment and the percentage of particle cluster coverage area to the total electrode area when different concentrations sample are applied to the transverse (3, 0) mode PRM. **b** Measured particle acoustic aggregation time in relation to the transverse mode order of PRM. **c**, **d** Particle enrichment duration as a function of input power and particle diameter corresponding to different transverse modes

evident that in four transverse modes, the microparticles are uniformly distributed at the center of the sector electrodes, indicating effective microparticle enrichment by the PRM across all four modes.

Interesting, the transverse (3,0) and (4,0) modes exhibit three distinct particle dynamic states when the excitation frequency is finely tuned: (State 1) Particles accumulate at the center of the sector electrode at higher resonant frequency f_1; (State 2) Particles undergo counterclockwise rotation when the frequency decreases from f_1 to f_2, with maximal rotational velocity observed near $(\frac{f1+f2}{2})$. This rotation reverses to clockwise when frequency increases from f_2 to f_1; (State 3): Particles migrate to the electrode edge at lower resonant frequency f_2 (where $f_1 > f_2$). Figure 5b systematically demonstrates these three enrichment states for the (3, 0) mode and confirms the rotational behavior (State 2) characteristic of the (4, 0) mode. The frequency-dependent reversal of rotational direction suggests asymmetric mode excitation during frequency tuning. While detailed mechanistic analysis remains a subject for future investigation, this phenomenon provides critical guidance for optimizing frequency tuning in the particle enrichment process.

Characterization of acoustofluidic performance of PRM

Next, we conducted a systematic study on the relationships between particle concentration and diameter, as well as the input excitation power and the duration of particle enrichment. We analyzed the impact of particle concentration on the percentage of focused particle cluster coverage area in the electrode region and compared the particle enrichment times across different transverse modes. The time required to complete particle enrichment was identified as one of the key qualitative criteria for assessing the acoustofluidic performance of PRM. The enrichment process is deemed complete when particle movement ceases and the size of each cluster, centered at the top, no longer undergoes significant changes. As shown in Fig. 6a, the duration of particle enrichment is proportional to the particle concentration, and there is an upper limit (approximately 50%) on the percentage of the electrode area occupied by particle

clusters. When the concentration is too high, the area occupied by particle clusters does not continue to increase. This is because, at elevated concentrations, particles tend to stack on top of already aggregated particles instead of congregating in the unoccupied sections of the electrode. As illustrated in Fig. 6b, we compared the acoustic enrichment time for PS particles varies among different transverse modes, where the acoustic enrichment time is shortest for the transverse (2, 0) mode and longest for the transverse (4, 0) mode.

The inversely proportional relationship between the particle aggregation duration and the input voltage under distinct transverse modes of the PRM is illustrated in Fig. 6c. For instance, when we used the transverse (3, 0) mode PRM to actuate the 9 μm PS particle, the acoustic enrichment time decreased from 55 s to 15 s as a result of increasing the input voltage from 16 V_{pp} to 24 V_{pp}. Meanwhile, the particle aggregation duration for different transverse modes follows the same trend presented in Fig. 6b. Similarly, Fig. 6d indicates that the particle aggregation duration is also inversely proportional to particle diameter across different transverse modes of the PRM. Taking the transverse (3, 0) mode as an example, with a constant input voltage of 20 V_{pp}, the acoustic enrichment duration is approximately 54 s for the small 2 μm PS particles, dropping to 12 s for larger 20 μm PS particles. In general, the particle aggregation duration of the (2, 0) mode was lower than that of the (3, 0) mode. The two modes exhibited approximately the same aggregation duration only for particles with a diameter of 20 μm. The curve associated with the (4, 0) mode reflects the longest enrichment times, followed by the curve of the (1, 0) mode.

Demonstration of acoustofluidic-enhanced mass sensing

Typically, the chip sample was mounted on the probe station, and electrical contact was made with each test piece via a GSG probe. The electrical characterization of the frequency response for all test pieces was conducted using a network analyzer. First, the frequency response of each resonator was measured in air to ensure the availability of the device. Subsequently, a 0.7 μL droplet of deionized water was pipetted onto the resonator's surface to measure its frequency response in water. The volume uncertainty of less than ±10% was verified by gravimetric calibration and is accounted for in the reported mass loading values. The signal generator parameters were adjusted to match the liquid-phase resonance frequency of the PRM, with the peak voltage set to 20 V_{pp}. Following this, the resonant frequency was fine-tuned downward (within a range of 5.5 kHz) to align with the actual frequency offset during continuous particle enrichment. Following this, a drop of 0.7 μL of SiO_2 particle solution was added to the resonator's surface, and then the high-voltage signal was activated to induce acoustic particle aggregation. The calculated actual mass and buoyant mass of SiO_2 particles in a 0.7 μL droplet (0.75 mg/mL concentration) are approximately 0.525 μg and 262.5 ng, respectively, with an estimated ±10% uncertainty. The formula is as follows:

$$m_b = m\left(1 - \frac{\rho_{water}}{\rho_{particle}}\right) \tag{6}$$

Where m is the actual mass, ρ_{water} is the density of water and $\rho_{particle}$ is the density of SiO_2. The frequency response of each resonator was then re-measured, thereby recording the frequency response with focused particle clusters. Thus, as shown in Fig. 7, by combining these measurements with the frequency response in water, the mass sensor map (and the aggregation map of SiO_2 particles in each transverse mode) was obtained. As previously mentioned, the resonant frequency of the transverse (0, 0) mode in water was too low to be measured, and the introduction of 0.525 μg of SiO_2 particles resulted in an insufficient shift in the resonant frequency of the piezoelectric film for the transverse (1, 0) mode, which was smaller than the experimental error, leading to low data reliability. Therefore, results for the transverse (0, 0) and (1, 0) modes have been omitted for such an application.

As plotted in Fig. 7, the liquid-phase electrical characterization of the PRM was performed for three higher-order transverse modes. Obviously, the measured resonance frequency shifts for the transverse modes (2, 0), (3, 0), and (4, 0) were 1.5 kHz, 3.0 kHz, and 5.3 kHz, respectively. Correspondingly, the fractional frequency shifts after particle focusing under three transverse modes are 0.1304%, 0.1621% and 0.2041%, respectively, relative to the state of the pure water droplet without particles. Multiple measurements, reproducibility and calibration curves characterizing frequency shifts across distinct modes were evaluated in S4. Based on the above results, we have verified the feasibility of calibrating the loading mass of the enriched particles based on the measured resonance frequency offset before and after the acoustofluidic actuation. Among these modes, the transverse (4, 0) mode exhibited the strongest resonant peak response in deionized water, which can be attributed to its highest liquid-phase Q among all tested transverse modes. The liquid-phase Q value directly correlates with the energy dissipation of the device. A higher Q value indicates lower vibrational energy loss, resulting in a larger resonant peak amplitude and narrower bandwidth. Therefore, the transverse (4, 0) mode demonstrates the best overall sensing performance. On the other hand, the transverse (3, 0) mode shows exceptional signal recognition capabilities, with a significantly improved parasitic feedback suppression effect compared to the other modes. As

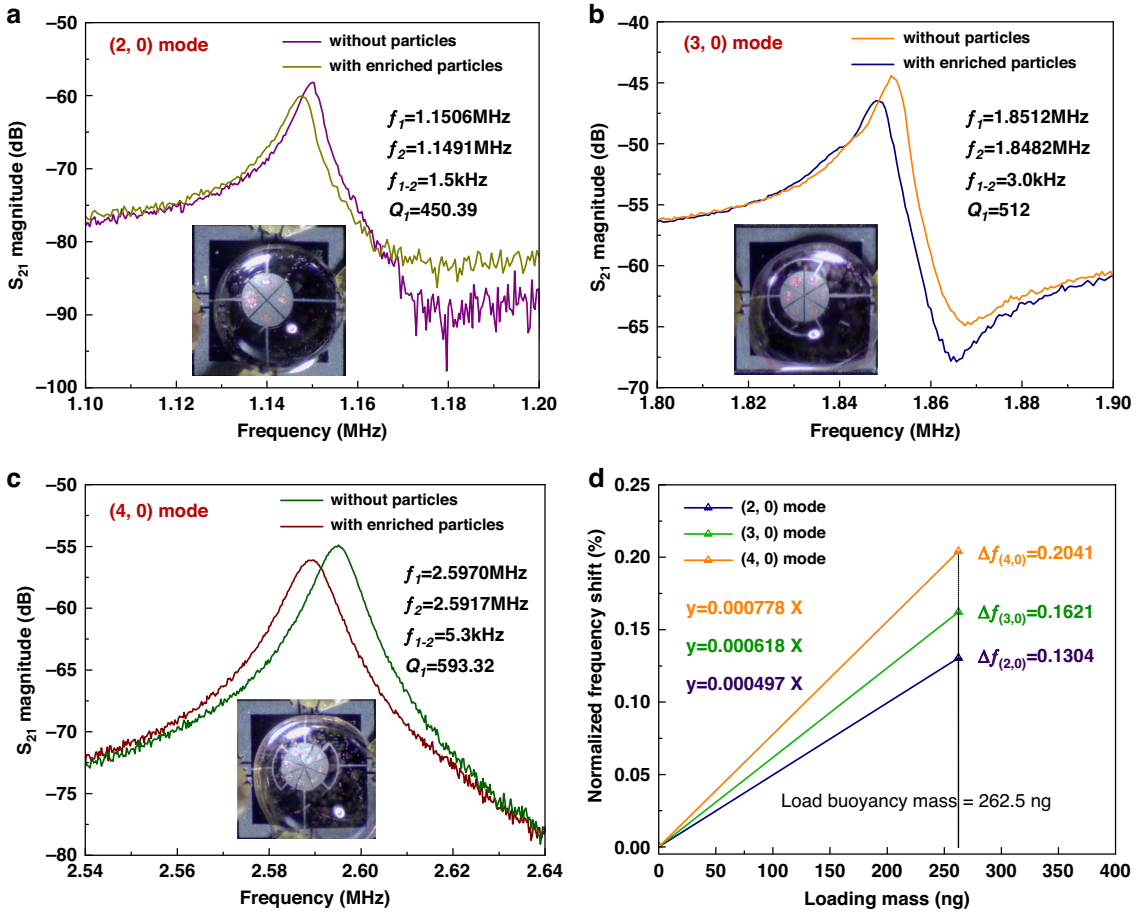

Fig. 7 Demonstration of multi-modal PRM for acoustofluidic enrichment and liquid-phase mass sensing of nanogram particles. a–c Results of frequency measurements of multimodal PRM under two different loading conditions in pure liquid and in focused particle clusters. The insert graphs represent acoustic enrichment results of 9 μm SiO_2 particles with a concentration of 0.75 mg/mL. **d** Comparison of resonant frequency shifts ratio of PRM caused by the same buoyancy mass load in different modes

illustrated in Fig. 7b, the resonant peak-to-feedthrough ratio (PFR) for the transverse (3, 0) mode is −67 dB. This high PFR value indicates strong separation between the resonant signal and parasitic interference, effectively reducing coupling noise caused by the high dielectric properties of the liquid phase. Consequently, the transverse (3, 0) mode exhibits superior anti-interference performance and delivers clearer, more stable resonant peak signals in complex liquid-phase environments. Besides, S_{21} amplitude variations for three transverse modes under uniform mass loading (see S5) reveal no statistical correlation between amplitude shifts and particle mass.

To analyze various internal and external measurement errors and interference conditions, we quantify the liquid-phase mass detection limit and evaluate resonant frequency stability using a transverse (3, 0) mode PRM. Notably, droplet evaporation is regarded as one of the influencing factors of measurement accuracy. As validated in S6 and S7, the total actuation and sensing duration is ≤99 s with droplet evaporation below 20% within 2 min, and such evaporation-induced temporal drift is effectively eliminated by time-dependent reference measurements performed on pure water droplets under identical experimental conditions. Beyond environmental disturbances, intrinsic frequency fluctuation constitutes the fundamental sensing limitation, which we suppressed and precisely characterized via continuous real-time frequency tracking enabled by a digitally configurable phase-locked loop instrument (HF2LI, Zurich Instruments) operating in self-oscillation mode. Further Allan deviation analysis confirms a frequency noise floor of 0.87 Hz (1σ), delivering a mass resolution of ~221 pg under the 3σ criterion and verifying the reliable nanogram-scale mass measurement capability of the PRM sensor (see S8).

High-order transverse resonant modes have theoretically demonstrated enhanced sensing sensitivity for resonant sensors. As previously established, increasing the modal order results in a greater number of divided fan-

shaped electrodes. LDV mode shape characterization reveals that the vibration amplitude is most pronounced near the central region of each sector electrode. As shown in Fig. 6a, the ratio of particle aggregation area to fan-shaped electrode area reaches saturation when particle concentration exceeds a critical threshold, indicating the robust acoustic enrichment capability of PRM. Notably, particles consistently preferentially aggregate at electrode centers regardless of concentration levels. Consequently, while higher-order resonances create more sector electrode divisions (i.e., additional aggregation centers), they simultaneously reduce the relative area of each aggregation center. This necessitates careful consideration of the sample concentration-electrode design matching relationship for resonant modes beyond (4, 0).

While liquid-phase mass sensing sensitivity is directly proportional to resonant frequency, miniaturizing the diaphragm diameter to elevate the resonant frequency presents significant challenges. Our prior investigation into the liquid-phase resonant characteristics of diaphragms with varying dimensions[8] revealed that reducing the PRM diameter to 360 μm increases the transverse (2, 0) mode resonant frequency to 2.82 MHz. However, this approach simultaneously leads to degradation in the quality factor and a corresponding increase in motional resistance, which contradicts the fundamental requirements for high-sensitivity sensing. Furthermore, experimental validation demonstrated that the PRM completely loses its liquid-phase functionality when the diameter is reduced below 260 μm[6]. These findings highlight the inherent limitations of geometric scaling for frequency enhancement, thereby underscoring the superior feasibility of the high-order resonant mode approach.

Conclusion

This work has examined a multiplicity of modes in piezoelectric resonant membranes that integrate acoustic particle manipulation and high-resolution mass sensing on a single micromechanical chip, overcoming critical limitations of conventional M/NEMS devices in liquid-phase resonance detection. Through systematic analysis of transverse vibration modes from (1, 0) to (4, 0), we demonstrate that the PRM enables spatially controlled particle enrichment with mode-dependent efficiency, where all the modes exhibit a unique inverse relationship between enrichment duration and input voltage/particle diameter. Critically, the ratio of particle cluster coverage area increases gradually as the concentration rises until it reaches approximately 50% (regarding as the acousto-fluidic limit value). Notably, the (4, 0) mode provides the best overall liquid-phase performance among tested modes with a quality factor of 247 and motional resistance of 31.69 kΩ, while the (3, 0) mode demonstrates exceptional signal fidelity with −67 dB parasitic feedthrough suppression, addressing long-standing challenges in liquid-phase signal extraction. By establishing a mode-specific performance optimization framework, this study enables application-driven design: the (4, 0) mode prioritizes energy efficiency for high-sensitivity detection, whereas the (3, 0) mode excels in noise immunity for precision measurements. The PRM's robust liquid-phase stability ($Q > 200$ across all modes), higher sensitivity and monolithic integration of actuation and sensing position it as a transformative platform for microanalyte detection in liquid phase. The present demonstration uses polystyrene microspheres and silica particles as model analytes. Extension to biological and environmental analytes with varying density and compressibility will require further characterisation of the acoustic contrast factor for each analyte class and is a direction for future work.

Acknowledgements

This work was supported by the National Natural Science Foundation of China under Grant Number 62301209 and 62431018, the Open Research Fund of State Key Laboratory of Millimeter Waves, Southeast University (No. K202502), the China Postdoctoral Science Foundation under Grant Number 2025M782891, and Anhui Postdoctoral Scientific Research Program Foundation No. 2026B1307.

Author details

[1]Anhui Province Key Laboratory of Measuring Theory and Precision Instrument, School of Instrument Science and Opto-Electronics Engineering, Hefei University of Technology, Hefei, China. [2]State Key Laboratory of Millimeter Waves, Southeast University, Nanjing, China. [3]School of Integrated Circuits, Wuhan University, Wuhan, China. [4]School of Electrical, Mechanical and Biomedical Engineering, University of Technology Sydney, Ultimo 2007, NSW, Australia. [5]Centre for Audio, Acoustics and Vibration, University of Technology Sydney, Ultimo 2007, NSW, Australia

Author contributions

J. Qian: Conceptualization, Writing-Review & Editing, Supervision, Project administration, Funding acquisition. W. Fan: Formal analysis, Investigation, Data Curation, Writing-Original Draft. C. Guo and S. Tang: Formal analysis, Investigation, Data Curation, Methodology. X. Wang and M. Huang: Validation, Visualization. G. Wu: Resources, Writing-Review & Editing. J. E.-Y. Lee: Methodology, Formal Analysis, Writing-Review & Editing.

Data availability

The data that support the findings of this study are available on request from the corresponding author.

Competing interests

The authors declare no competing interests.

Supplementary information The online version contains supplementary material available at https://doi.org/10.1038/s41378-026-01474-z.

Received: 1 April 2026 Revised: 3 August 2026 Accepted: 14 September 2026
Published online: 19 October 2026

References

1. Toledo, J. et al. Flow-through sensor based on piezoelectric MEMS resonator for the in-line monitoring of wine fermentation. *Sens. Actuators B Chem.* **254**, 291–298 (2018).
2. Burg, T. P. et al. Weighing of biomolecules, single cells and single nanoparticles in fluid. *Nature* **446**, 1066–1069 (2007).

3. Sage, E. et al. Single-particle mass spectrometry with arrays of frequency-addressed nanomechanical resonators. *Nat. Commun.* **9**, 3283 (2018).
4. Chaste, J. et al. A nanomechanical mass sensor with yoctogram resolution. *Nat. Nanotechnol.* **7**, 301–304 (2012).
5. Lin, A. T.-H., Yan, J. & Seshia, A. A. Electrically addressed dual resonator sensing platform for biochemical detection. *J. Microelectromech. Syst.* **21**, 34–43 (2012).
6. Qian, J., Begum, H. & Lee, J. E.-Y. Acoustofluidic localization of sparse particles on a piezoelectric resonant sensor for nanogram-scale mass measurements. *Microsyst. Nanoeng.* **7**, 61 (2021).
7. Qian, J. et al. Integrated functions of microfluidics and gravimetric sensing enabled by piezoelectric driven microstructures. *Appl. Phys. Rev.* **12**, 011401 (2025).
8. Begum, H., Qian, J. & Lee, J. E.-Y. Fully differential higher order transverse mode piezoelectric membrane resonators for enhanced liquid-phase quality factors. *J. Micromech. Microeng.* **31**, 104004 (2021).
9. Bhattacharya, S. & Li, S.-S. A fully differential SOI-MEMS thermal piezoresistive ring oscillator in liquid environment intended for mass sensing. *IEEE Sens. J.* **19**, 7261–7268 (2019).
10. Lee, J. E.-Y. & Seshia, A. A. Parasitic feedthrough cancellation techniques for enhanced electrical characterization of electrostatic microresonators. *Sens. Actuators A Phys.* **156**, 36–42 (2009).
11. Waggoner, P. S. & Craighead, H. G. Micro- and nanomechanical sensors for environmental, chemical, and biological detection. *Lab Chip* **7**, 1238–1255 (2007).
12. Qaradaghi, V. et al. Surface area enhancement of nanomechanical disk resonators using MWCNT for mass-sensing applications. *IEEE Trans. Ultrason. Ferroelectr. Freq. Control* **66**, 609–615 (2019).
13. Mahdavi, M., Abbasalipour, A. & Pourkamali, S. Thin film piezoelectric-on-silicon elliptical resonators with low liquid phase motional resistances. *IEEE Sens. J.* **19**, 113–120 (2019).
14. Weckman, N. E. & Seshia, A. A. Reducing dissipation in piezoelectric flexural microplate resonators in liquid environments. *Sens. Actuators A Phys.* **267**, 464–473 (2017).
15. Patocka, F. et al. Novel resonant MEMS sensor for the detection of particles with dielectric properties in aged lubricating oils. *Sens. Actuators A Phys.* **315**, 112290 (2020).
16. Corbin, E. A. et al. Measuring physical properties of neuronal and glial cells with resonant microsensors. *Anal. Chem.* **86**, 4864–4872 (2014).
17. Pinto, R. M. R. et al. Thin-film silicon MEMS for dynamic mass sensing in vacuum and air: phase noise, Allan deviation, mass sensitivity and limits of detection. *J. Microelectromech. Syst.* **28**, 390–400 (2019).
18. Bryan, A. K., Goranov, A., Amon, A. & Manalis, S. R. Measurement of mass, density, and volume during the cell cycle of yeast. *Proc. Natl. Acad. Sci. USA* **107**, 999–1004 (2010).
19. Qaradaghi, V. et al. Nanoelectromechanical disk resonators as highly sensitive mass sensors. *IEEE Electron Device Lett.* **39**, 1744–1747 (2018).
20. Schmid, U. & Schneider, M. High performance piezoelectric ALN MEMS resonators for liquid sensing and beyond-the potential of piezomems. In *Proc. 2019 20th International Conference on Solid-State Sensors, Actuators and Microsystems & Eurosensors XXXIII* (TRANSDUCERS & EUROSENSORS XXXIII) 653–654 (IEEE, 2019).
21. Begum, H., Qian, J. & Lee, J. E.-Y. Effect of crystal orientation on liquid phase performance of piezoelectric-on-silicon elliptical plate resonators. *Sens. Actuators A Phys.* **340**, 113548 (2022).
22. Lin, Z. W., Wu, C. Y. & Li, S. S. Feedthrough engineering to enable resonant sensors working in conductive medium for bio applications. *J. Microelectromech. Syst.* **33**, 333–341 (2024).
23. Toledo, J. et al. Piezoelectric MEMS resonators for cigarette particle detection. *Micromachines* **10**, 145 (2019).
24. Wang, N., Kanhere, E., Triantafyllou, M. S. & Miao, J. M. Shark-inspired MEMS chemical sensor with epithelium-like micropillar electrode array for lead detection. In *Proc. 2015 18th Int. Conf. Solid-State Sensors, Actuators Microsyst. (TRANSDUCERS)* 1464–1467 (IEEE, Anchorage, AK, USA, 2015).
25. Qian, J., Begum, H. & Lee, J. E.-Y. Acoustic centrifugation facilitating particle sensing in liquid on a piezoelectric resonator. *IEEE Electron Device Lett.* **43**, 801–804 (2022).
26. Daryani, M. M., Manzaneque, T., Wei, J. & Ghatkesar, M. K. Measuring nanoparticles in liquid with attogram resolution using a microfabricated glass suspended microchannel resonator. *Microsyst. Nanoeng.* **8**, 92 (2022).
27. Ombati, N. W., Kahmann, T., Viereck, T. & Peiner, E. MEMS-based cantilever sensor for simultaneous measurement of mass and magnetic moment of magnetic particles. *Chemosensors* **9**, 207 (2021).
28. Wu, M. et al. Acoustofluidic separation of cells and particles. *Microsyst. Nanoeng.* **5**, 32 (2019).
29. Gu, Y. et al. Acoustofluidic holography for micro- to nano- scale particle manipulation. *ACS Nano* **14**, 14635–14645 (2020).
30. Cheng, C. Y. et al. Thin film PZT-based PMUT arrays for deterministic particle manipulation. *IEEE Trans. Ultrason. Ferroelectr. Freq. Control* **66**, 1606–1615 (2019).
31. Vachon, P. et al. Microfabricated acoustofluidic membrane acoustic waveguide actuator for highly localized in-droplet dynamic particle manipulation. *Lab Chip* **23**, 1865–1878 (2023).
32. Arcamone, J. et al. Efficient capacitive transduction of high-frequency micromechanical resonators by intrinsic cancellation of parasitic feedthrough capacitances. *Appl. Phys. Lett.* **97**, 043505 (2010).
33. Samarasekera, C. et al. Trapping, separating, and palpating microbead clusters in droplets and flows using capacitive micromachined ultrasonic transducers (CMUTs). *Sens. Actuators B Chem.* **276**, 481–488 (2018).
34. Qian, J. et al. Low-cost laser-cut patterned chips for acoustic concentration of micro-to nanoparticles and cells by operating over a wide frequency range. *Analyst* **146**, 3280–3288 (2021).
35. Abdolvand, R. et al. Micromachined resonators: a review. *Micromachines* **7**, 160 (2016).
36. Petean, P. G. C. & Aguiar, M. L. Determining the adhesion force between particles and rough surfaces. *Powder Technol.* **274**, 67–76 (2015).
37. Rajupet, S., Sow, M. & Lacks, D. J. Particle adhesion to rough surfaces. *Phys. Rev. E* **102**, 012904 (2020).
38. Li, Y. et al. Recent progress in field-directed assembly of colloids in an evaporating droplet. *Adv. Mater. Interfaces* **12**, 2401869 (2025).
39. Gesing, A., Platz, D. & Schmid, U. Viscous fluid–structure interaction of micro-resonators in the beam–plate transition. *J. Appl. Phys.* **131**, 134502 (2022).